


Cite this: *Mater. Adv.*, 2024,  
5, 5772Received 24th February 2024,  
Accepted 7th June 2024

DOI: 10.1039/d4ma00189c

rsc.li/materials-advances

# Accelerated design of L<sub>12</sub>-strengthened single crystal high entropy alloys based on machine learning and multi-objective optimization

Wenchao Yang, \* Shunsheng Lin, Qiang Wang, Chen Liu, Jiarun Qin and Jun Zhang\*

A comprehensive strategy of machine learning and multi-objective optimization based on thermodynamic simulation data was proposed to accelerate the composition design of L<sub>12</sub>-strengthened single crystal high entropy alloys (SX-HEAs). This approach simultaneously optimized various alloy microscopic parameters, such as volume fraction and solvus temperature of L<sub>12</sub> phase, TCP phase content, liquidus–solidus temperatures, and density, using a machine learning model. From a pool of 2 515 661 candidates, a composition of Ni<sub>41.5</sub>Co<sub>31</sub>Cr<sub>8</sub>Ti<sub>4</sub>Al<sub>10</sub>W<sub>0.5</sub>Mo<sub>2</sub>Ta<sub>3</sub> (at%) was selected and then the related microscopic parameters were verified experimentally with a high accuracy. Furthermore, the designed alloy reached a yield strength of 873 MPa at 800 °C and 503 MPa at 1000 °C, as well as a creep life of 111.65 h at 1038 °C/158.6 MPa and 62.67 h at 1038 °C/172 MPa. This material design strategy based on machine learning and multi-objective optimization extends the L<sub>12</sub>-strengthened SX-HEAs design method to optimize simultaneously multiple objectives, rather than one by one.

## 1. Introduction

High entropy alloys (HEAs)<sup>1–4</sup> were a new alloy system based on configuration entropy principal alloy, which was considered one of the most promising alloys. This design concept broke the traditional alloy design concept of traditional metallic materials with single principal elements, showing the unique physical and mechanical properties.<sup>5–7</sup> Among them, the coherent strengthening between the L<sub>12</sub>-type nanoparticles and FCC matrix showed the most promising strengthening effect to maintain the excellent mechanical properties over a wide temperature range.<sup>8–10</sup>

However, the composition of multiple elements (Ti, Al, W, Mo, *etc.*) was crucial in determining the volume fraction of the L<sub>12</sub> phase. An excessive increase in certain elements (such as Mo and W) could result in the formation of TCP phases (such as  $\sigma$ ,  $\eta$ ,  $\mu$ , Laves, *etc.*) in HEAs.<sup>3,11–13</sup> Additionally, it was worth noting that many L<sub>12</sub>-type nanoparticles could only maintain a thermal stability at relatively low temperatures (below 850 °C), which limited their potential for practical applications. This had been observed in the Al<sub>0.5</sub>CrCuNiCoFe HEAs system, where the L<sub>12</sub> phase solvus temperature ranged from 800 °C to 850 °C.<sup>14</sup> Furthermore, the current research on L<sub>12</sub>-strengthened HEAs has mainly focused on the polycrystalline structure. However,

the polycrystalline HEAs also exhibited intergranular embrittlement like most structural materials. The phenomenon was particularly evident at intermediate temperatures, where polycrystalline materials tended to experience severe intergranular embrittlement due to stress-assisted oxygen infiltration along grain boundaries, leading to premature failure. These issues greatly hindered the widespread use of HEAs, especially in harsh environments. Notably, the synthesis of single crystals offered a promising solution for eliminating the negative effects of grain boundaries and had the potential to significantly improve the alloy's temperature capacity and high-temperature service performance.<sup>15–18</sup> Therefore, it was of great significance to design the composition of L<sub>12</sub>-strengthened single crystal high entropy alloys (SX-HEAs).

The design of high-performance HEAs for L<sub>12</sub>-strengthened SX-HEAs presented a significant challenge due to the diverse range of alloy elements, composition, and single-crystal processing technology. Traditional trial-and-error or intuitive methods were often ineffective in this context. Therefore, it was necessary to find a more efficient and accelerated manner to discover multi-component HEAs with satisfactory multi-performance. In the past few decades, machine learning (ML) had increasingly been used in materials science research because of its efficient computational and predictive capabilities.<sup>19–26</sup> For example, Zheng *et al.*<sup>18</sup> for the first time innovatively used an experimental nickel-based database for ML to design and prepare HEAs with expected L<sub>12</sub> phase volume fraction (> 55%) and tensile strength (> 1 GPa) in Al–Co–Cr–Fe–Ni–Ti six-element system. Liu *et al.*<sup>26</sup>

State Key Laboratory of Solidification Processing, Northwestern Polytechnical University, Xi'an 710072, China. E-mail: wenchao yang@nwpu.edu.cn, zhjsscott@nwpu.edu.cn; Fax: +86-29-88492228; Tel: +86-29-88492228



aimed to find HEAs with high  $L_{12}$  phase volume fraction and high hardness by establishing prediction models for multilayer structures, including precise prediction models for microstructure parameters and hardness properties. It was important to note that in the cases mentioned above, the design of HEAs often prioritizes a single microstructure parameter and room temperature performance. In the case of  $L_{12}$ -strengthened SX-HEAs, it was crucial to accurately predict and characterize their properties under various high-temperature conditions, as well as their physical properties that reflected their performances at elevated temperatures. However, when the performance of  $L_{12}$ -enhanced SX-HEAs was in conflict, it was not possible to consider a single ML model at the same time. Instead, multiple ML models must be constructed in order to optimize the performance one by one. To optimize the overall performance of a material, it was inevitable to face multiple constraints and property conflicts. Notably, the multi-objective optimization approach could effectively address the non-linear and multi-dimensional aspects of the alloy design problem.<sup>27</sup>

In this work, based on the calculation data established by the thermodynamic Pandat software, an ML model was built for the relationship of  $L_{12}$ -strengthened SX-HEAs between compositions and  $L_{12}$  phase volume fraction ( $V_{L_{12}}$ ),  $L_{12}$  phase solvus temperature ( $T_{L_{12}}$ ), TCP phase content after heat treatment (TCP), solidus temperature ( $T_S$ ), liquidus temperature ( $T_L$ ) and density ( $\rho$ ). A multi-objective screening and optimization process was developed for SX-HEAs by means of alloy composition design guidelines and material structure reverse design concepts. The reasonableness of the SX-HEA composition design method and the alloy design criteria in this work was indirectly verified by testing the microcosmic parameters of the designed alloy. Concurrently, the reliability of the design criteria was verified through tensile and creep tests conducted at elevated temperatures. The method would broaden the idea for the composition design of  $L_{12}$ -strengthened single crystal HEAs in the future.

## 2. Method

### 2.1 Calculation method

**2.1.1 Design strategy.** A design strategy based on machine learning and multi-objective optimization was applied to optimize multiple performance parameters of  $L_{12}$ -strengthened SX-HEAs, including  $V_{L_{12}}$ ,  $T_{L_{12}}$ , TCP,  $T_S$ ,  $T_L$ , and  $\rho$ . The design workflow of  $L_{12}$ -strengthened SX-HEAs was shown in Fig. 1. The composition space of 8 elements (Ni, Co, Cr, Ti, Al, W, Mo, and Ta) was set for the  $L_{12}$ -strengthened SX-HEAs. Furthermore, 271 compositions were randomly sampled from Pandat, a thermodynamic software was used to calculate the equilibrium phase content and the transition temperature of the phase transition. After comparing the errors of various machine learning algorithms, the optimal model for training was used to establish the mapping relationship between the components and each target parameter. In addition, the method was also used for multi-objective search in the range of interest. To further optimize the multi-objective, the range of output

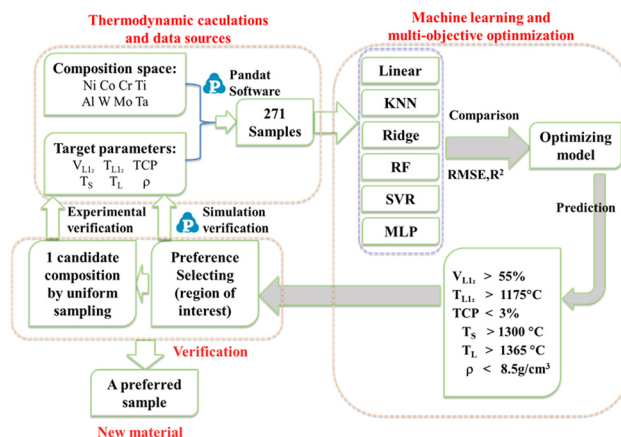


Fig. 1 Design workflow of  $L_{12}$ -strengthened SX-HEAs aided by machine learning and multi-objective optimization.

parameters was limited, and the optimization results were substituted back to Pandat software to verify the effect of machine learning prediction. By analyzing the occurrence frequency of alloying elements and comparing the influence law of the variation of alloying elements on the output parameters, the alloy composition for the test was obtained. Finally, the reliability of the designed alloy was verified by experiments.

**2.1.2 Dataset.** Reasonable and reliable data sources were the basis for effective machine learning. However, the experimental data of  $L_{12}$ -strengthened HEAs were insufficient, especially, since the high-temperature properties were rarely reported in related literature. In this work, based on the successful experience of Joseph *et al.*<sup>28</sup> in designing HEAs through thermodynamic simulation, the relevant data set of Ni-Co-Cr-Ti-Al-W-Mo-Ta 8-element HEAs system was constructed by using the thermodynamic simulation software Pandat. The chosen database for this article was PanNi-2016, which contained all though the necessary elements to construct the dataset. It was important to mention that this study aimed to design alloys with excellent mechanical properties at high temperatures, however, the Pandat thermodynamics software did not include the calculation of these properties. Based on the successful experience of Liu *et al.*<sup>29</sup> in designing  $L_{12}$ -strengthened new cobalt-based superalloys, the selection of output parameters in this work was based on their research. The rationality of the alloy design was indirectly explained by the intrinsic parameters of the material at high temperatures. Firstly, the alloying element content and step size were limited to the following ranges: Co: 20–45 at%, Cr: 7–25 at%, Ti: 0–10 at%, Al: 0–10 at%, W: 0.5–1.5 at%, Mo: 0–5 at%, Ta: 0–3 at%, with a step size of 0.5 for W and 1 for the remaining elements. Additionally, the Ni content was kept within the range of 20–45 at%. This resulted in a total of 2 515 661 alloy compositions to be predicted. However, using the thermodynamic software Pandat to calculate all of these components would be time-consuming. Therefore, in this work, based on the reported distribution characteristics of alloy components,<sup>2,3,6–8,14</sup> 271 components were randomly selected, including the phase content of the equilibrium state at 900 °C, and finally established surrogate models through ML.



**2.1.3 Machine learning strategy.** In this work, linear regression (Linear), *K*-nearest neighbor regression (KNN), ridge regression (Ridge), random forest regression (RF), support vector regression model (SVR), and multi-layer sensor regression (MLP) were used to build surrogate models, respectively. Six different regression models were trained with  $V_{L1_2}$ ,  $T_{L1_2}$ , TCP,  $T_s$ ,  $T_L$ , and  $\rho$  as the multi-task outputs respectively. The alloy compositions were used as input for each ML model. The sample data was divided into two subsets, which were the training set (70%) and the test set (30%). The performances of the models were comprehensively measured by root mean square error (RMSE) and  $R^2$  score, expressed in eqn (1) and (2), respectively.

$$\text{RMSE} = \sqrt{\frac{\sum_{i=1}^m (y_i - \hat{y}_i)^2}{m}} \quad (1)$$

$$R^2 = 1 - \frac{\sum_{i=1}^m (y_i - \hat{y}_i)^2}{\sum_{i=1}^m (y_i - \bar{y}_i)^2} \quad (2)$$

where  $y_i$  represented for the observation value of the  $i$ -th sample,  $\hat{y}_i$  stood for the predicted value of the  $i$ -th sample, and  $\bar{y}_i$  was the average of the observation value. In addition,  $m$  was the number of data samples. The smaller the RMSE, the model error would be smaller. The  $R^2$  within [0,1] was an evaluating indicator to represent for the proportion of response variation “explained” by the regressors.

**2.1.4 Multi-objective optimization.** The optimization objectives and constraints were determined based on domain knowledge and aimed at finding globally suitable candidate compositions. The predefined preferences for the optimized objectives, namely  $V_{L1_2}$ ,  $T_{L1_2}$ ,  $T_s$ , and  $T_L$ , were set to be greater than 55%, 1175 °C, 1300 °C, and 1365 °C, respectively. The constraint thresholds for TCP and  $\rho$ , were set to be lower than 3% and 8.5 g cm<sup>-3</sup>, respectively. An optimal combination of components was then identified that satisfied all of the above objectives and constraints. By analyzing the occurrence frequency of alloying elements and their influence on the output parameters, the alloy composition for testing was determined. Finally, the rationality of the alloy composition was verified through tests of microscopic parameters and mechanical properties.

## 2.2 Experimental procedure

One candidate composition obtained by ML and multi-objective optimization was verified by experiments. Raw metals with a purity higher than 99.9% were applied. Alloy button ingots were prepared by vacuum arc melting. To ensure the uniformity of the alloy composition, the alloy was melted at least 6 times per 100 g and homogenized by the magnetic stirring of the vacuum electric arc furnace. Then the button ingots were directionally solidified into [001] single crystal rod by high-rate solidification (HRS) technology at a withdrawal rate of 100  $\mu\text{m s}^{-1}$ . The heat treatment regime of the alloy was 1220 °C/1 h + 1230 °C/2 h + 1240 °C/2 h + 1250 °C/4 h A.C. + 1050 °C/4 h A.C. The density of

the alloy was determined by the Archimedean drainage method. The transformation temperatures were measured by differential scanning calorimetry (DSC)-STA449F3 within the high-purity Ar flow. The sample in 3 mm × 3 mm × 0.5 mm for DSC was tested within the temperature range of 600–1400 °C at a heating rate of 20 °C min<sup>-1</sup>. The linear interpolation method was employed to measure  $T_{L1_2}$ ,  $T_s$ , and  $T_L$  based on the DSC heating curves. The etched chemically with the solution of HNO<sub>3</sub>:HF:C<sub>3</sub>H<sub>8</sub>O<sub>3</sub> in volume ratio of 1:2:3. The microstructures were characterized by TESCAN Clara GMH scanning electron microscope (SEM) and Leica DM3000 optical microscopy (OM). Rod specimens with diameter of 3 mm and standard distance of 15 mm were used to evaluate their tensile properties. Uniaxial tensile tests were conducted at a nominal strain rate of  $2.5 \times 10^{-3} \text{ s}^{-1}$  along the [001] direction in the temperature range from RT to 1000 °C, such as 800 °C, 900 °C, and 1000 °C. Rod specimens with a diameter of 5 mm and a standard distance of 25 mm were used to evaluate their tensile properties. A set of uniaxial constant loading tensile creep tests was accomplished at 1038 °C/158.6 MPa, and 1038 °C/172 MPa. All the creep tests were carried out in a TM105-A1 creep testing machine.

## 3. Results and discussion

### 3.1 Establishments of ML and multi-objective optimization

**3.1.1 Establishment and evaluation of regression model.** Fig. 2 showed that  $R^2$  and RMSE values were obtained from training six models with 6 output parameters. It was clear that the RF model had the highest  $R^2$  value, exceeding 0.95 for five of the output parameters:  $V_{L1_2}$ ,  $T_{L1_2}$ , TCP,  $T_s$ , and  $T_L$  (Fig. 2a). Additionally, the RMSE of the RF model was smaller than that of the other 5 models (Fig. 2b). While the Linear model had the highest  $R^2$  value and the smallest RMSE for the output parameter of  $\rho$ , these values did not significantly outperform those of the RF model. It indicated that the RF model should be most suitable for the 6 data sets used in this work. Therefore, the RF model was selected as the prediction model for all six output parameters in this work.

**3.1.2 Alloy compositions search space.** After establishing the machine learning model, it could be used to predict the composition of unknown alloys. Then, a multi-objective optimization strategy was applied to find the alloy components that meet the desired output parameters. Fig. 3 illustrated the search space of the L1<sub>2</sub>-strengthened HEAs comprehensive prediction system used. According to the requirements in the figure, the

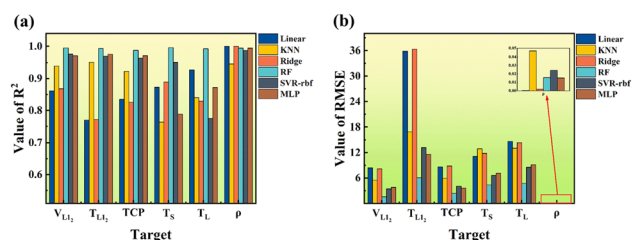


Fig. 2 Performance evaluation of 6 regression models: (a)  $R^2$ ; (b) RMSE.



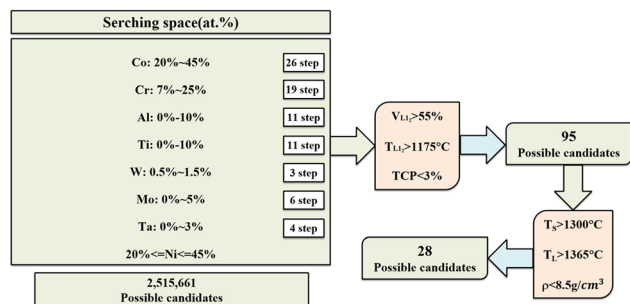


Fig. 3 Search space of comprehensive prediction system for  $L_{12}$ -strengthened SX-HEAs.

alloy element content and step size were limited, and the total number of alloy components could be predicted to be 2 515 661. It was worth noting that the content of each element was limited to 45 at% to ensure the predicted alloy components fall within the reasonable range for HEAs. Additionally, according to previous research by Liu *et al.*,<sup>26</sup> the content of Ti and Al were the forming elements of the  $L_{12}$  phase, which should be restricted to 10 at% to prevent a phase transition from FCC to BCC in the alloy.<sup>24,30</sup> The objective of this work was to enhance the mechanical properties of HEAs at high temperatures by adding appropriate refractory elements such as W, Mo and Ta. Therefore, a multi-objective optimization process was conducted for all alloy components within the predicted measurement space. Initially, the criteria of  $V_{L_{12}} > 55\%$ ,  $T_{L_{12}} > 1175^\circ\text{C}$ , and  $\text{TCP} < 3\%$  were imposed, resulting in the identification of 95 potential alloy components. This step was crucial in the development of an alloy that could maintain a high-volume fraction of the  $L_{12}$  phase and exhibit the structural stability under high-temperature conditions. Subsequently, the criteria of  $T_s > 1300^\circ\text{C}$ ,  $T_L > 1365^\circ\text{C}$ , and  $\rho < 8.5\text{ g cm}^{-3}$  were applied, leading to the selection of 28 alloy compositions. This step was essential in designing an alloy with excellent performance at high temperatures and ensured its practical application in engineering.

**3.1.3 Computational verification.** Although the prediction of large component space by machine learning ultimately selected 28 candidate alloy components, the accuracy of predicting unknown alloy components by ML was not clear. Therefore, the Pandat software was utilized again to validate the effectiveness of the ML method on 28 alloy components. Besides, Fig. 4 illustrated

the comparison between the predicted and calculated values of the output parameters. On the whole, the ML model performed well in predicting the 6 output parameters, and the predicted values were in good agreement with the calculated values of Pandat software, indicating that the RF model could predict these 6 output parameters in alloys with high accuracy.<sup>2,6,29,31</sup>

**3.1.4 Occurrence frequency of alloying element content.** In the previous section, 28 candidate alloys were identified using machine learning and multi-objective optimization strategies. However, it was not feasible to experimentally verify all 28 alloys simultaneously. Therefore, this section focused on analyzing the frequency of occurrence of the 28 alloy elements to narrow down the selection of experimental alloys, and the results were illustrated in Fig. 5.<sup>18</sup>

On the one hand, the distribution of Ni, Co, Cr, and Ti (Fig. 5a–d) in the alloy was uneven, with no clear advantage in the occurrence frequency of any one element. This work focused on the design of  $L_{12}$ –( $\text{Ni}_3\text{Al}$ ) type precipitated phase.<sup>6</sup> The content of Ni in the final alloy was over 40 at%, and the content of Co was between 27 at% and 32 at%. The sum of the content of the two elements accounted for about 3/4, which should occupy the central position of the 6 faces of the  $\text{Ni}_3\text{Al}$  structure. Similarly, the elements Cr and Ti should occupy 8 corner positions of the  $\text{Ni}_3\text{Al}$  structure.<sup>6</sup> The above results also verified the reliability of ML methods in alloy design and alloy screened.

On the other hand, the Al and W contents were fixed at 10 at% and 0.5 at%, respectively (Fig. 5e and f). The Al was the formed element of the  $L_{12}$ –( $\text{Ni}_3\text{Al}$ ) type precipitated phase, and the content of Al in the 28 candidate alloys in this example was 10 at%, indicating that increased the Al content would also increase the volume fraction of the  $L_{12}$  phase. The W element played a crucial role in improving the high-temperature performance of the alloy. In this work, the search range for W content was set at 0.5–1.5 at% (Fig. 3) to enhance the high-temperature

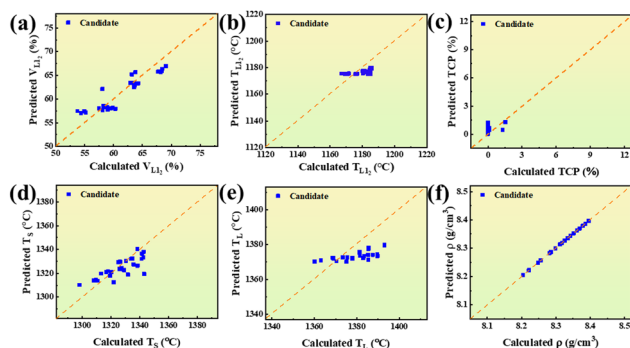


Fig. 4 Comparisons of the optimization values by RF and the calculation values by Pandat software: (a)  $V_{L_{12}}$ ; (b)  $T_{L_{12}}$ ; (c) TCP; (d)  $T_s$ ; (e)  $T_L$ ; (f)  $\rho$ .

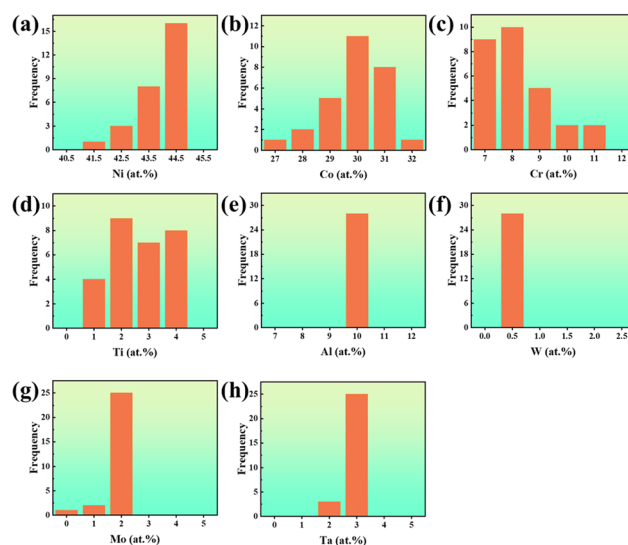


Fig. 5 Frequency maps of the filtered 28 alloys composition: (a)–(h) were the frequency maps of Ni, Co, Cr, Ti, Al, W, Mo, and Ta, respectively.





performance of the final designed alloy. However, in this particular example, the W content in the final screened alloy composition was fixed at 0.5 at% due to the synergistic effects it had on the 6 output parameters. The increase of W content further would make it difficult to achieve the multi-objective optimization design objectives.

Finally, Mo and Ta had the highest frequencies when the content of Mo and Ta appeared at 2 at% and 3 at%, respectively (Fig. 5g and h). As a refractory element, Mo also played an important role in improving high-temperature performance. However, when its content was too high, the TCP phase might be precipitated on the matrix, thus significantly damaging the high-temperature durability of the alloy.<sup>32</sup> According to machine learning, the comprehensive sensitivity of Mo to the range of 6 output parameters was highest at 2 at%, while no relevant component occurred at 3–5 at%. No related components were found in 3–5 at%, indicating that the further increase of Mo element promoted the precipitation of the TCP phase. Pandey *et al.*<sup>6</sup> promoted the L1<sub>2</sub> phase solvus temperature of the HEAs to 1156 °C by addition of 2.8 at% Ta element. In this work, the alloy selection was carried out by ML, and the final occurrence frequency of Ta element was 3 at%, indicating that the addition of Ta not only increased the L1<sub>2</sub> phase solvus temperature in the alloy but also made the comprehensive sensitivity to meet the requirements of the range of 6 output parameters the highest.

In summary, the contents of Al, W, Mo, and Ta were fixed at 10 at%, 0.5 at%, 2 at%, and 3 at%, respectively, based on the results and discussion in this section. However, the contents of the other four elements have not yet been determined. Further analysis would be conducted in the next section to determine the final experimental composition.

**3.1.5 Influence of element content variation on output parameters.** The effect of element content on the 6 output parameters was illustrated in Fig. 6. As the Ni content increased,  $V_{L1_2}$  initially decreased and then slightly increased (Fig. 6a), while  $T_s$ ,  $T_L$ , and  $\rho$  first increased and then decreased (Fig. 6d–f). However,  $T_{L1_2}$  and TCP in the alloy had a minimal impact (Fig. 6b and c). On the other hand, increased Co content led to an initial increase in  $V_{L1_2}$  followed by a decrease, and a decrease in TCP (Fig. 6a and c). The  $T_s$  and  $T_L$  in the alloy increased (Fig. 6d and e), while the  $T_{L1_2}$  (Fig. 6b) remained relatively

unchanged and  $\rho$  (Fig. 6f) fluctuated. When the Cr content increased,  $V_{L1_2}$  decreased (Fig. 6a),  $T_{L1_2}$  fluctuated within a range of 2 °C without significant change (Fig. 6b), TCP increased (Fig. 6c),  $T_s$  initially increased and then decreased (Fig. 6d),  $T_L$  decreased (Fig. 6e), and  $\rho$  showed fluctuations (Fig. 6f). Finally, increasing Ti content increased  $V_{L1_2}$  (Fig. 6a), with  $T_{L1_2}$  remained relatively unchanged within a range of 2 °C (Fig. 6b), a decrease in TCP (Fig. 6c), a decrease in  $T_s$  (Fig. 6d), and fluctuations in  $T_L$  temperature within a range of 2 °C (Fig. 6e). The  $\rho$  showed a clear decreased trend (Fig. 6f).

According to the rule of the influence of alloying element content on 6 output parameters, this work selected 28 alloy components to verify the alloy composition. The goal was to minimize the content of the Ni element, maximize the content of the Co element, minimize the content of the Cr element, and maximize the content of the Ti element. The aim was to ensure that the final selected alloy would have high values for  $V_{L1_2}$ ,  $T_{L1_2}$ ,  $T_s$ ,  $T_L$ , and low values for TCP and  $\rho$ . After considered the practical situation of the 28 alloy compositions, the study determined the composition of the tested alloy to be Ni<sub>41.5</sub>Co<sub>31</sub>Cr<sub>8</sub>Ti<sub>4</sub>Al<sub>10</sub>W<sub>0.5</sub>Mo<sub>2</sub>Ta<sub>3</sub> (at%).

## 3.2 Experimental verification

**3.2.1 Microscopic parameters.** After using ML to select an alloy component, the microscopic parameters of the alloy were experimentally tested to indirectly verify its high-temperature mechanical properties. Ni<sub>41.5</sub>Co<sub>31</sub>Cr<sub>8</sub>Ti<sub>4</sub>Al<sub>10</sub>W<sub>0.5</sub>Mo<sub>2</sub>Ta<sub>3</sub> SX-HEA microscopic parameters of the test results were shown in Fig. 7. An optical microscopy image of the designed as-cast SX-HEA microstructure in this work was shown in Fig. 7a. The microstructure was arranged in a “cross-petal” morphology. Meanwhile, the primary dendrite arm spacing in the as-cast structure was 280 μm. Fig. 7b and c displayed the thermodynamic equilibrium phase diagram and DSC heating curve of the SX-HEA, respectively. From the equilibrium phase diagram, it could be observed that there were three-phase transition temperatures at 1168 °C, 1298 °C,

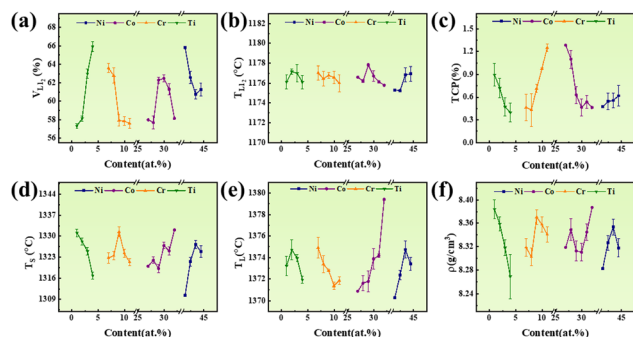


Fig. 6 The influence of element content change on all targets: (a)  $V_{L1_2}$ ; (b)  $T_{L1_2}$ ; (c) TCP; (d)  $T_s$ ; (e)  $T_L$ ; (f)  $\rho$ .

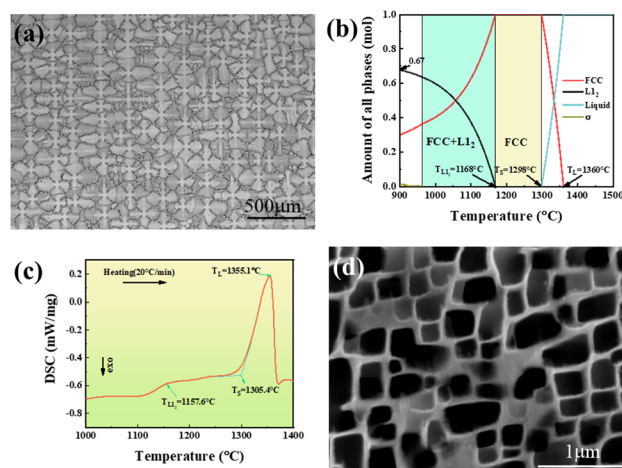


Fig. 7 Test results of microscopic parameters of Ni<sub>41.5</sub>Co<sub>31</sub>Cr<sub>8</sub>Ti<sub>4</sub>Al<sub>10</sub>W<sub>0.5</sub>Mo<sub>2</sub>Ta<sub>3</sub> SX-HEA: (a) optical microscopy image of the as-cast SX-HEA showing dendritic and inter-dendritic regions; (b) pandat phase diagram based on SX-HEA nominal composition; (c) DSC heating curve of the as-cast SX-HEA; (d) SEM micrograph of SX-HEA after heat treatment.



**Table 1** Comparison of experimental, Pandat, and ML test results

| Result                       | Experimental | Pandat | ML   |
|------------------------------|--------------|--------|------|
| $V_{L_{12}}$ (%)             | 68           | 67     | 66   |
| $T_{L_{12}}$ (°C)            | 1157.6       | 1168   | 1175 |
| TCP (%)                      | 0            | 0.54   | 0.46 |
| $T_s$ (°C)                   | 1305.4       | 1298   | 1310 |
| $T_L$ (°C)                   | 1355.1       | 1360   | 1370 |
| $\rho$ (g cm <sup>-3</sup> ) | 8.45         | 8.41   | 8.43 |

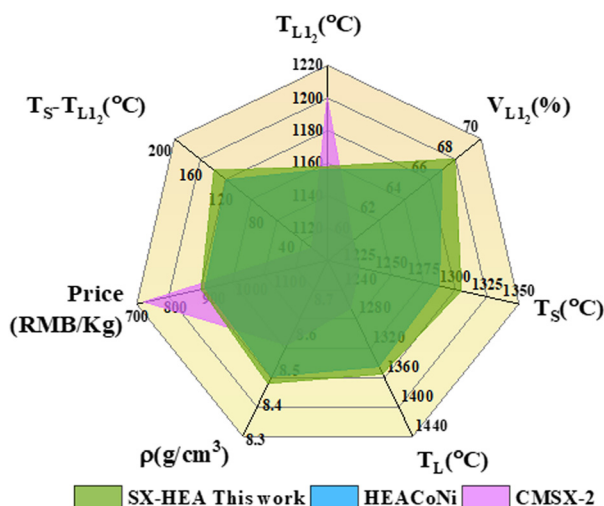
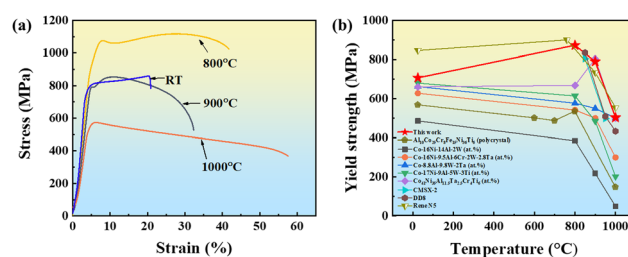
and 1360 °C, respectively. The DSC heating curve revealed three-phase transition temperatures:  $T_{L_{12}}$ ,  $T_s$ , and  $T_L$ , which were 1157.6 °C, 1305.4 °C, and 1355.1 °C, respectively. Fig. 7d showed the microstructure of the final selected SX-HEA after heat treatment. After statistical analysis using Image-J software, it was found that the  $L_{12}$  phase volume fraction in the SX-HEA after heat treatment was 68%. Additionally, there was no TCP phase precipitation observed in the alloy microstructure after heat treatment. The density of the alloy was determined to be 8.45 g cm<sup>-3</sup> used the Archimedeian drainage method.

By comparing the results of the experiment, thermodynamic Pandat software, and ML, as shown in Table 1, it could be seen that the differences among the three results were within a reasonable range. It was similar to the results of Deng *et al.*<sup>32</sup> Furthermore, the above results showed that machine learning using thermodynamic software was reasonable, and its prediction results could effectively guide the alloy design.

In addition, the properties of the alloys designed in this work were compared with those of other alloys. A radar diagram comparing the various properties of the design alloy with HEA CoNi and CMSX-2 was shown in Fig. 8.<sup>6,33,34</sup> The SX-HEAs developed in this work outperforms HEA CoNi (Co<sub>37.6</sub>Ni<sub>35.4</sub>Al<sub>9.9</sub>Mo<sub>4.9</sub>Cr<sub>5.9</sub>Ta<sub>2.8</sub>Ti<sub>3.5</sub>) in all the properties displayed in the figure, while also reducing cost and density. Compared to the first-generation nickel-based single-crystal superalloy CMSX-2, HEA showed better performance in all areas except  $T_{L_{12}}$  and price. Overall, significant improvements had been achieved in

terms of performance when compared to the CMSX-2 alloy. Notably, SX-HEA had a lighter density than CMSX-2 (SX-HEA: 8.45 g cm<sup>-3</sup>, CMSX-2: 8.56 g cm<sup>-3</sup>). In the aviation industry, reducing weight had always been a sought-after goal.

**3.2.2 Mechanical properties.** The tensile experiments of SX-HEA at different temperatures were carried out, the results were displayed in Fig. 9. Fig. 9a showed the engineering stress-strain curves of the designed SX-HEA at different temperatures. The specific values were shown in Table 2. It could be observed that the yield strength of the alloy increases significantly at 800 °C compared to room temperature. Specifically, the yield strength was 873 MPa at 800 °C and 707 MPa at room temperature, respectively. However, as the temperature increased, the yield strength of the alloy decreased. The properties of the alloy did not decrease significantly after the temperature increased. The yield strength maintained 503 MPa at 1000 °C. The anomalous yield temperature of nickel-based superalloy was about 800 °C.<sup>35</sup> It had also been observed in some HEAs.<sup>36,37</sup> It was caused by thermally activated cross-slip dislocation of the octahedral {111} vertical aspect {100} in the optimal  $L_{12}$  phase.<sup>38</sup> Fig. 9b showed the yield strength comparison between the SX-HEA designed in this work, partial polycrystalline high-entropy alloy, and single-crystal alloy at different temperatures. It was worth noting that compared with polycrystalline high-entropy alloys and new cobalt-based single-crystal superalloys reported in recent years,<sup>39–42</sup> the designed alloys had superior tensile properties at room temperature to 1000 °C, especially at high temperatures above 800 °C. Furthermore, when compared to the SX-HEA,<sup>17</sup> the designed alloy showed better tensile properties at room temperature and 800 °C. At 900 °C and 1000 °C, the tensile properties of the designed alloy were comparable to those of the designed alloys. Additionally, compared to the nickel-based single-crystal superalloys CMSX-2 and DD8,<sup>43,44</sup> the designed alloy exhibited greater advantages in

**Fig. 8** Radar diagram of SX-HEA, HEA CoNi, and CMSX-2 on multiple properties.<sup>6,33,34</sup>**Fig. 9** Tensile curves and performances comparison of SX-HEA: (a) stress-strain curves of SX-HEA at RT, 800 °C, 900 °C, 1000 °C; (b) yield strength of SX-HEA at different temperatures, compared with that of polycrystalline HEAs and other single crystal nickel-based superalloys, cobalt-based superalloys and HEAs.<sup>17,38–44</sup>**Table 2** Tensile properties of SX-HEA at different temperatures

| Temperature (°C) | YS (MPa) | UTS (MPa) | $\phi$ (%) |
|------------------|----------|-----------|------------|
| RT               | 707      | 860       | 17         |
| 800              | 873      | 1117      | 35         |
| 900              | 790      | 854       | 28         |
| 1000             | 503      | 571       | 54         |

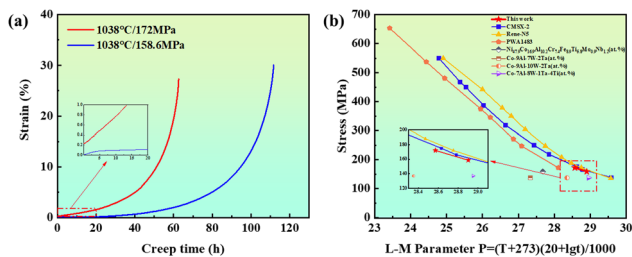


Fig. 10 Creep fracture curves and performances comparison of SX-HEA: (a) Overall strain-creep curves of SX-HEA at 1038 °C/158.6 MPa and 1038 °C/172 MPa; (b) Comparison of L-M coefficients between SX-HEA and some alloys.<sup>45–50</sup>

tensile properties at high temperatures. Similarly, when compared to Rene N5, the second-generation nickel-based single-crystal superalloy,<sup>45</sup> the designed alloy showed certain advantages at 900 °C, which was essentially equivalent at 800 °C. In summary, the final alloy selected by the machine learning method in this work had good comprehensive tensile properties and a certain high temperature application potential.

In addition, the creep performances of SX-HEA were also tested. The creep properties of SX-HEA at 1038 °C/158.6 MPa and 1038 °C/172 MPa were shown in Fig. 10a. Under these two conditions, the creep life was 111.65 h and 62.67 h, and the fracture elongation was 30.12% and 27.26%, respectively. To evaluate the creep properties of SX-HEA, nickel-based single-crystal superalloys, novel cobalt-based single-crystal superalloys, and published L<sub>12</sub>-strengthened SX-HEA were selected for comparison. Fig. 10b showed L-M curves of different alloys (L-M coefficient ( $P = (T + 273)(20 + \lg t)/1000$ ), where  $T$  was the experimental temperature and  $t$  was the creep rupture life). In this paper, the L-M coefficients of SX-HEA at 1038 °C/158.6 MPa and 1038 °C/172 MPa were 28.91 and 28.51, respectively. Compared with the SX-HEA,<sup>46</sup> the first-generation nickel-based single crystal superalloy PWA-1483,<sup>47</sup> and the new cobalt-based single crystal superalloys,<sup>48,49</sup> the L-M coefficient points of SX-HEA were on the right or above, indicating that the designed alloy had the better creep properties than the above alloys. At the same time, the L-M coefficient points of the designed alloy were close to that of the first generation single crystal CMSX-2, and slightly to the left of the second generation single crystal Rene N5 L-M coefficient point,<sup>50,51</sup> indicating that the creep performance of SX-HEA was the same as that of the first generation single crystal CMSX-2 and slightly lower than Rene N5. Considering that the density of CMSX-2 was 8.56 g cm<sup>-3</sup> and the density of the alloy designed in this work was 8.45 g cm<sup>-3</sup>, the alloy designed in this work still had the characteristics of low density under the condition of basically equivalent performance, and it had a certain application potential.

## 4. Conclusion

In this work, a design strategy based on ML and multi-objective optimization was proposed for the discovery of a new L<sub>12</sub>-strengthened SX-HEA. The conclusions were drawn as follows.

(1) By using the RF model and combining the design criteria of  $V_{L12}$ ,  $T_{L12}$ , TCP,  $T_s$ ,  $T_L$ , and  $\rho$ , one alloy was selected from 2515661 alloys. The experimental results showed that the surrogate model based on error evaluation had high accuracy. The  $V_{L12}$ ,  $T_{L12}$ , TCP,  $T_s$ ,  $T_L$  and  $\rho$  in Ni<sub>41.5</sub>Co<sub>31</sub>Cr<sub>8</sub>Ti<sub>4</sub>Al<sub>10</sub>W<sub>0.5</sub>Mo<sub>2</sub>Ta<sub>3</sub> (at%) were 68%, 1157.6 °C, 0%, 1305.4 °C, 1355.1 °C and 8.45 g cm<sup>-3</sup>, respectively.

(2) The yield strength of SX-HEA was 873 MPa and 503 MPa at 800 °C and 1000 °C, respectively. The creep life at 1038 °C/158.6 MPa and 1038 °C/172 MPa were 111.65 h and 62.67 h, respectively. The mechanical properties were of SX-HEAs better than some single-crystal alloys.

(3) This material design strategy based on ML and multi-objective optimization extended the L<sub>12</sub>-strengthened SX-HEAs design method to optimize multiple targets simultaneously, rather than one by one. At the same time, the design concept and theoretical results of auxiliary alloys would provide important guidance for the further study of new L<sub>12</sub>-strengthened SX-HEAs.

## Data availability statements

The data that support the findings of this study are available from the corresponding author upon request.

## Conflicts of interest

The authors declare that they have no known competing financial interests or personal relationships that could have appeared to influence the work reported in this paper.

## Acknowledgements

This work was funded by the National Natural Science Foundation of China (52322410, 52071263, 52031012); Self-innovation Special Fund Project of Aero Engine Corporation of China (ZZCX-2022-040); The Key Research and Development Program of Shaanxi Province (2023-YBGY-432); Research Fund of the State Key Laboratory of Solidification Processing (NPU), China (2021-QZ-03) and Science Center for Gas Turbine Project (P2021-A-IV-001-001).

## References

- 1 J. W. Yeh, S. K. Chen, S. J. Lin, J. Y. Gan, T. S. Chin, T. T. Shun, C. H. Tsau and S. Y. Chang, Nanostructured high-entropy alloys with multiple principal elements: novel alloy design concepts and outcomes, *Adv. Eng. Mater.*, 2004, **6**, 299–303.
- 2 Y. F. Ye, Q. Wang, C. T. Liu and Y. Yang, High-entropy alloy: challenges and prospects, *Mater. Today*, 2016, **19**, 349–362.
- 3 T. Yang, Y. Zhao, W. Liu, J. Kai and C. Liu, L<sub>12</sub>-strengthened high-entropy alloys for advanced structural applications, *J. Mater. Res.*, 2018, **33**, 2983–2997.
- 4 Z. P. Lu, H. Wang, M. W. Chen, I. Baker, J. W. Yeh, C. T. Liu and T. G. Nieh, An assessment on the future development of





- high-entropy alloys: Summary from a recent workshop, *Intermetallics*, 2015, **66**, 67–76.
- 5 T. Yang, Y. L. Zhao, B. X. Cao, J. J. Kai and C. T. Liu, Towards superior mechanical properties of hetero-structured high-entropy alloys via engineering multicomponent intermetallic nanoparticles, *Scr. Mater.*, 2020, **183**, 39–44.
  - 6 P. Pandey, S. Kashyap, D. Palanisamy, A. Sharma and K. Chattopadhyay, On the high temperature coarsening kinetics of  $\gamma'$  precipitates in a high strength  $\text{Co}_{37.6}\text{Ni}_{35.4}\text{Al}_{9.9}\text{Mo}_{4.9}\text{Cr}_{5.9}\text{Ta}_{2.8}\text{Ti}_{3.5}$  fcc-based high entropy alloy, *Acta Mater.*, 2019, **177**, 82–95.
  - 7 Y. L. Zhao, Y. R. Li, G. M. Yeli, J. H. Luan, S. F. Liu, W. T. Lin, D. Chen, X. J. Liu, J. J. Kai, C. T. Liu and T. Yang, Anomalous precipitate-size-dependent ductility in multicomponent high-entropy alloys with dense nanoscale precipitates, *Acta Mater.*, 2022, **223**, 117480.
  - 8 J. Y. He, H. Wang, Y. Wu, X. J. Liu, H. H. Mao, T. G. Nieh and Z. P. Lu, Precipitation behavior and its effects on tensile properties of FeCoNiCr high-entropy alloys, *Intermetallics*, 2016, **79**, 41–52.
  - 9 J. Y. He, H. Wang, H. L. Huang, X. D. Xu, M. W. Chen, Y. Wu, X. J. Liu, T. G. Nieh, K. An and Z. P. Lu, A precipitation-hardened high-entropy alloy with outstanding tensile properties, *Acta Mater.*, 2016, **102**, 187–196.
  - 10 Y. L. Zhao, T. Yang, Y. R. Li, L. Fan, B. Han, Z. B. Jiao, D. Chen, C. T. Liu and J. J. Kai, Superior high-temperature properties and deformation-induced planar faults in a novel  $\text{L}_{12}$ -strengthened high-entropy alloy, *Acta Mater.*, 2020, **188**, 517–527.
  - 11 J. X. Hou, B. X. Cao, B. Xiao, Z. B. Jiao and T. Yang, Compositionally complex coherent precipitation-strengthened high-entropy alloys: a critical review, *Rare Met.*, 2022, **41**, 2002–2015.
  - 12 B. Cao, T. Yang, W. Liu and C. T. Liu, Precipitation-hardened high-entropy alloys for high-temperature applications: A critical review, *MRS Bull.*, 2019, **44**, 854–859.
  - 13 Y. L. Zhao, T. Yang, Y. Tong, J. Wang, J. H. Luan, Z. B. Jiao, D. Chen, Y. Yang, A. Hu, C. T. Liu and J. J. Kai, Heterogeneous precipitation behavior and stacking-fault-mediated deformation in a CoCrNi-based medium-entropy alloy, *Acta Mater.*, 2017, **138**, 72–82.
  - 14 N. G. Jones, A. Frezza and H. J. Stone, Phase equilibria of an  $\text{Al}_{0.5}\text{CrFeCoNiCu}$  high entropy alloy, *Mater. Sci. Eng. A*, 2014, **615**, 214–221.
  - 15 Z. Wan, L. Hu, Y. Sun, T. Wang and Z. Li, Microstructure evolution and dynamic softening mechanisms during high-temperature deformation of a precipitate hardening Ni-based superalloy, *Vacuum*, 2018, **155**, 585–593.
  - 16 E. I. Galindo-Nava and P. E. J. Rivera-Díaz-del-Castillo, *Thermodynamical modelling of hot deformation in FCC metals*, in *J. Plast.*, 2013, **47**, pp. 202–221.
  - 17 W. C. Xiao, S. F. Liu, Y. L. Zhao, J. J. Kai, X. J. Liu and T. Yang, A novel single-crystal  $\text{L}_{12}$ -strengthened Co-rich high-entropy alloy with excellent high-temperature strength and antioxidant property, *J. Mater. Res. Technol.*, 2023, **23**, 2343–2350.
  - 18 S. G. Ma, S. F. Zhang, M. C. Gao, P. K. Liaw and Y. Zhang, A successful synthesis of the  $\text{CoCrFeNiAl}_{0.3}$  single-crystal, high-entropy alloy by Bridgman solidification, *JOM*, 2013, **65**, 1751–1758.
  - 19 T. Zheng, X. Hu, F. He, Q. Wu, B. Han, C. Da, J. Li, Z. Wang, J. Wang, J. Kai, Z. Xia and C. T. Liu, Tailoring nanoprecipitates for ultra-strong high-entropy alloys via machine learning and prestrain aging, *J. Mater. Sci. Technol.*, 2021, **69**, 156–167.
  - 20 W. Huang, P. Martin and H. L. Zhuang, Machine-learning phase prediction of high-entropy alloys, *Acta Mater.*, 2019, **169**, 225–236.
  - 21 C. Wen, Y. Zhang, C. Wang, D. Xue, Y. Bai, S. Antonov, L. Dai, T. Lookman and Y. Su, Machine learning assisted design of high entropy alloys with desired property, *Acta Mater.*, 2019, **170**, 109–117.
  - 22 Y. J. Chang, C. Y. Jui, W. J. Lee and A. C. Yeh, Prediction of the composition and hardness of high-entropy alloys by machine learning, *JOM*, 2019, **71**, 3433–3442.
  - 23 Y. Zhang, C. Wen, C. Wang, S. Antonov, D. Xue, Y. Bai and Y. Su, Phase prediction in high entropy alloys with a rational selection of materials descriptors and machine learning models, *Acta Mater.*, 2020, **185**, 528–539.
  - 24 X. Liu, J. Zhang and Z. Pei, Machine learning for high-entropy alloys: Progress, challenges and opportunities, *Prog. Mater. Sci.*, 2023, **131**, 101018.
  - 25 Q. Han, Z. Lu, S. Zhao, Y. Su and H. Cui, Data-driven based phase constitution prediction in high entropy alloys, *Comp. Mater. Sci.*, 2022, **215**, 111774.
  - 26 W. Liu, C. Wang, C. Liang, J. Chen, H. Tan, J. Yang, M. Liang, X. Li, C. Liu, M. Huang and X. Liu, Optimal design of  $\gamma'$ -strengthened high-entropy alloys via machine learning multi-layer structural model, *Mater. Sci. Eng., A*, 2023, **871**, 144852.
  - 27 A. Gaspar-Cunha and J. A. Cova, Robustness in multi-objective optimization using evolutionary algorithms, *Comput. Optim. Appl.*, 2008, **39**, 75–96.
  - 28 J. Joseph, M. Annasamy, S. R. Kada, P. D. Hodgson, M. R. Barnett and D. M. Fabijanic, Optimising the Al and Ti compositional window for the design of  $\gamma'$  ( $\text{L}_{12}$ )-strengthened Al–Co–Cr–Fe–Ni–Ti high entropy alloys, *Mater. Sci. Eng., A*, 2022, **835**, 142620.
  - 29 P. Liu, H. Huang, S. Antonov, C. Wen, D. Xue, H. Chen, L. Li, Q. Feng, T. Omori and Y. Su, Machine learning assisted design of  $\gamma'$ -strengthened Co-base superalloys with multi-performance optimization, *npj Comput. Mater.*, 2020, **6**, 62.
  - 30 T. Borkar, B. Gwalani, D. Choudhuri, C. V. Mikler, C. J. Yannetta, X. Chen, R. V. Ramanujan, M. J. Styles, M. A. Gibson and R. Banerjee, A combinatorial assessment of  $\text{Al}_x\text{CrCuFeNi}_2$  ( $0 < x < 1.5$ ) complex concentrated alloys: Microstructure, microhardness, and magnetic properties, *Acta Mater.*, 2016, **116**, 63–76.
  - 31 Y. Deng, Y. Zhang, X. Gong, W. Hu, Y. Wang, Y. Liu and L. Lian, An intelligent design for Ni-based superalloy based on machine learning and multi-objective optimization, *Mater. Des.*, 2022, **221**, 110935.
  - 32 B. X. Cao, T. Yang, L. Fan, J. H. Luan, Z. B. Jiao and C. T. Liu, Refractory alloying additions on the thermal stability and





- mechanical properties of high-entropy alloys, *Mater. Sci. Eng., A*, 2020, **797**, 140020.
- 33 T. Grosdidier, A. Hazotte and A. Simon, Precipitation and dissolution processes in  $\gamma/\gamma'$  single crystal nickel-based superalloys, *Mater. Sci. Eng., A*, 1998, **256**, 183–196.
  - 34 M. Okazaki, M. Sakaguchi and R. Kamma, Early growth of creep-fatigue small cracks in an advanced cast Ni-based superalloys, *Trans. Indian Inst. Met.*, 2010, **63**, 259–263.
  - 35 R. C. Reed, *The superalloys: fundamentals and applications*, Cambridge university press, 2008.
  - 36 H. M. Daoud, A. M. Manzoni, N. Wanderka and U. Glatzel, High-temperature tensile strength of  $\text{Al}_{10}\text{Co}_{25}\text{Cr}_8\text{Fe}_{15}\text{Ni}_{36}\text{Ti}_6$  compositionally complex alloy (high-entropy alloy), *JOM*, 2015, **67**, 2271–2277.
  - 37 T. K. Tsao, A. C. Ye, C. M. Ku and H. Murakami, On the superior high temperature hardness of precipitation strengthened high entropy Ni-based alloys, *Adv. Eng. Mater.*, 2017, **19**, 1600475.
  - 38 A. Korner, H. P. Karnthaler and C. Hitznerberger, Transmission electron microscopy study of cross-slip and of Kear-Wilsdorf locks in  $\text{L}_{12}$  ordered  $\text{Ni}_3\text{Fe}$ , *Philos. Mag. A*, 1987, **56**, 73–88.
  - 39 N. Petrushin, K. Hvatzkiy, V. Gerasimov, T. Link, A. Epishin, G. Nolze and G. Gerstein, A Single-Crystal Co-Base Superalloy Strengthened by  $\gamma'$  Precipitates: Structure and Mechanical Properties, *Adv. Eng. Mater.*, 2015, **17**, 755–760.
  - 40 L. Shi, J. J. Yu, C. Y. Cui and X. F. Sun, Temperature dependence of deformation behavior in a Co-Al-W-base single crystal superalloy, *Mater. Sci. Eng., A*, 2015, **620**, 36–43.
  - 41 L. Klein, Y. Shen, M. S. Killian and S. Virtanen, Effect of B and Cr on the high temperature oxidation behaviour of novel  $\gamma/\gamma'$ -strengthened Co-base superalloys, *Corros. Sci.*, 2011, **53**, 2713–2720.
  - 42 L. Shi, J. J. Yu, C. Y. Cui and X. F. Sun, Effect of Ta additions on microstructure and mechanical properties of a single-crystal Co-Al-W-base alloy, *Mater. Lett.*, 2015, **149**, 58–61.
  - 43 P. J. Cong, J. S. Hou, L. Z. Zhou, Z. M. Ren and J. T. Guo, Effects of disorientation on tensile properties of hot corrosion resistant single crystal superalloy DD483, *Chin. J. Nonferrous Met.*, 2001, **21**, 747–753.
  - 44 F. R. N. Nabarro and F. De Villiers, *Physics of creep and creep-resistant alloys*, CRC press, 2018.
  - 45 J. Corrigan, M. G. Launsbach and J. R. Mihalisin, *Nickel base superalloy and single crystal castings*, US Pat 8241560 B2, 2012.
  - 46 T. K. Tsao, A. C. Yeh, C. M. Kuo, K. Kakehi, H. Murakami, J. W. Yeh and S. R. Jian, The high temperature tensile and creep behaviors of high entropy superalloy, *Sci. Rep.*, 2017, **7**, 12658.
  - 47 D. M. Shah and A. Cetel, Evaluation of PWA1483 for large single crystal IGT blade applications, *Superalloys.*, 2000, **2000**, 295–304.
  - 48 F. Xue, H. J. Zhou and Q. Feng, Improved high-temperature microstructural stability and creep property of novel Co-base single-crystal alloys containing Ta and Ti, *JOM*, 2014, **66**, 2486–2494.
  - 49 S. Lu, S. Antonov, L. Li, C. Liu, X. Zhang, Y. Zheng, H. L. Fraser and Q. Feng, Atomic structure and elemental segregation behavior of creep defects in a Co-Al-W-based single crystal superalloys under high temperature and low stress, *Acta Mater.*, 2020, **190**, 16–28.
  - 50 J. Gong, D. Snyder, T. Kozmel, C. Kern, J. E. Saal, I. Berglund, J. Sebastian and G. Olson, ICME design of a castable, creep-resistant, single-crystal turbine alloy, *JOM*, 2017, **69**, 880–885.
  - 51 J. B. Wahl and K. Harris, *New single crystal superalloys, CMSX<sup>®</sup>-8 and CMSX<sup>®</sup>-7*. American Society of Mechanical Engineers, 2014, 45752, V006T22A002.

